HiSST: 2nd International Conference on
High-Speed Vehicle Science Technology
20–24 April 2020, Bruges, Belgium

CHARACTERIZATION OF SCRAMJET INTAKE FLOWFIELDS AND PERFORMANCE DURING ASCENT FLIGHT VIA HIGH-RESOLUTION NUMERICAL SIMULATION

Chihiro Fujio[1], Shuvayan Brahmachary[2], Hideaki Ogawa[3]

Abstract

Scramjets are one of the most promising propulsion technologies for efficient and flexible space transportation. However, rather few studies have been reported for scramjets specifically for ascending flight, which is of crucial importance to realise space transportation. Axisymmetric intake flowfields are investigated numerically assuming a typical scramjet operation on a constant dynamic pressure ascent trajectory, aiming to achieve scramjet-powered access-to-space. Physical insight into scramjet flowfields at various flight altitudes and Mach numbers have been obtained by means of high-fidelity numerical simulation using adaptive mesh refinement. The intake performance is evaluated with respect to the compression efficiency, drag, the temperature at the intake exit. The insight gained here can be usefully applied to the design of high-performance scramjet intakes for ascent trajectories.

Keywords: scramjet engine, hypersonic airbreathing propulsion, ascent flight, scramjet intake, computational fluid dynamics

Nomenclature

M_∞ – Freestream Mach number
p_∞ – Freestream static pressure (Pa)
T_∞ – Freestream static temperature (K)
$\bar{M}_2$ – Stream-thrust averaged Mach number at the intake exit
$\bar{p}_2$ – Stream-thrust averaged static pressure at the intake exit (Pa)
$\bar{p}_{t2}$ – Stream-thrust averaged total pressure at the intake exit (Pa)
$\bar{T}_2$ – Stream-thrust averaged static temperature at the intake exit (K)

1. Introduction

Scramjet (supersonic combustion ramjet) engines are a promising hypersonic airbreathing technology that can fulfil the increasing requirements of space transportation due to advantages in numerous aspects over conventional propulsion systems. The reusability of scramjet-powered vehicles without the need to carry oxidizers warrants significant cost reduction, as compared to rockets. The relatively simple design and mechanism without involving moving parts unlike turbojet engines offer advantages in terms of safety and manufacture. Due to these attractive characteristics of scramjet engines, numerous studies have been conducted so far, with significant progress made in the last two decades, achieving various remarkable milestones including: the first in-flight supersonic combustion in the HyShot II program in July 2002 [1], the fastest flight at Mach 9.6 by X-43 in the Hyper-X program in November 2014 [2], and the longest-duration flight by Boeing X-51A in May 2010.

Scramjet engines typically operate in a sequential process: hypersonic inflow is compressed to desirable pressure and temperature through the intake. Following fuel injection, the gas mixture is burned at the

[1] *Department of Aeronautics and Astronautics, Kyushu University, 744 Motooka, Nishi-ku, Fukuoka 819-0395, Japan, fujio.chihiro.354@s.kyushu-u.ac.jp*
[2] *Department of Aeronautics and Astronautics, Kyushu University, 744 Motooka, Nishi-ku, Fukuoka 819-0395, Japan, brahmachary.shuvayan.140@m.kyushu-u.ac.jp*
[3] *Department of Aeronautics and Astronautics, Kyushu University, 744 Motooka, Nishi-ku, Fukuoka 819-0395, Japan, hideaki.ogawa@aero.kyushu-u.ac.jp*

combustor. The reacted gas is expanded through the nozzle and accelerated to produce thrust. Internal flow including complicate phenomena is a dominant factor that critically determines the performance of scramjet engines, thus rendering high-performance intake design crucial for the success of scramjets.

Axisymmetric scramjet configuration can bring about numerous advantages over complex three-dimensional geometries in aerodynamic and combustion efficiency, aerothermal and structural management as well as manufacture. Also, combined with innovative concepts such as upstream fuel injection [3,4] and radical farming [5,6], axisymmetric scramjets are considered to offer promise for excellent performance. However, axisymmetric scramjet inlets with high internal compression are inherently difficult to start spontaneously. To avoid unstart, various techniques have been examined numerically. In particular, instantaneous diaphragm rapture with bleed addition and sliding have been found to be effective in starting the inlets [7]. Despite these efforts, detailed investigation of the internal flowfield of scramjet intakes remains of crucial importance for the successful development and operation of scramjet engines, especially for ascending flights.

In ascending flight, the inflow condition varies drastically with altitude and velocity, and the angle of attack causes the internal flow of axisymmetric intakes to be no longer axisymmetric. This may result in undesirable effects such as inadequate compression, increased drag, nonuniform flow downstream, and intake unstart in a severe case, while flow spillage may facilitate intake starting albeit reduced mass flow. Further, the adequately large thrust must be produced to overcome the gravity and drag forces. These complications represent a challenge for scramjet-powered access-to-space.

In hypersonic operation, the trajectories of scramjet-powered ascent flights are typically designed, assuming in constant dynamic pressure in consideration of two limitations; thermal and structural limitation as a lower limitation, and; combustion stability consideration as an upper limitation. To reach the suitable hypersonic flow condition, other propulsion systems such as rocket, ramjet and turbojet engines can be adapted as the first stage of the scramjet-powered space transportation system.

In this paper, an axisymmetric scramjet intake flowfield in various altitudes is numerically investigated, assuming typical scramjet operation on a constant dynamic pressure trajectory, with focus on the flow characteristics and performance. The intake performance is evaluated by measuring quantities such as compression ratio, total pressure recovery and drag. Physical insights are gained into underlying flow mechanism by probing into the steady viscous flowfields by means of high-fidelity computational fluid dynamics by using high-resolution adaptive mesh refinement.

2. Methodologies

2.1. Configurations

A three-ramp axisymmetric configuration (Fig. 1) is employed for the scramjet intake in this study to achieve compression adequately and efficiently, based on a previous study by Ogawa et al. 2010 [8]. This configuration is represented by eight geometric parameters: the leading-edge nose-tip radius r_t, ramp lengths $l_{1,2,3}$, first ramp angle θ_1, ramp angle increments $\Delta\theta_{2,3}$, inlet radius r_i, and exit radius r_c (or combustor entrance radius). In conjunction with these parameters, the geometry is defined with the following values: $r_\mathrm{t} = 0.5\ \mathrm{mm}$, $l_1 = 0.204\ \mathrm{m}$, $l_2 = 0.069\ \mathrm{m}$, $l_3 = 0.039\ \mathrm{m}$, $\theta_1 = 5.0°$, $\Delta\theta_2 = 5.3°$, $\Delta\theta_3 = 3.3°$, $r_\mathrm{i} = 0.075\ \mathrm{m}$, and $r_\mathrm{c} = 0.035\ \mathrm{m}$. A small degree of divergence is applied to the combustor section downstream to impose a throat condition at the intake exit and ensure a supersonic flow downstream.

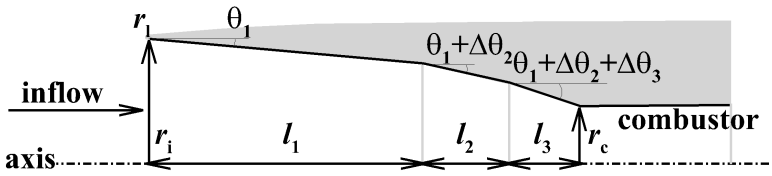

Fig. 1. Schematic of a three-ramp axisymmetric intake

The freestream conditions are calculated assuming a typical scramjet operation on a constant dynamic pressure trajectory of 53.6 kPa. In particular, the flow conditions at three altitudes (shown in Table 1)

are considered in this investigation, while the angle of attack is fixed at 0°, thus the flowfields remain axisymmetric.

Table 1. Freestream conditions

Altitude [km]	M_∞	p_∞ [Pa]	T_∞ [K]
30.0	8	1197	226.5
31.6	9	946	228
33.0	10	766	231

2.2. Computational Fluid Dynamics

Intake flowfields are computed by using the density-based continuum commercial CFD solver ANSYS Fluent 19.1 [9]. An implicit scheme with second-order spatial accuracy is used to solve the Navier-Stokes equations for steady flowfields. The full multigrid technique is adapted to accelerate convergence. The airflow is treated as a calorically perfect gas with a constant specific heat ratio of 1.4. The boundary layer is assumed to be turbulent, modelled by the 2-equation k-ω SST model [10]. The inlet surface is assumed to be an isothermal wall at 300K. Further, an adiabatic wall condition at the altitude of 30 km at Mach 8 is also examined to show the effect of wall boundary conditions. The energy residual is converged to the order of 10^{-6}.

A fully structured (quadrilateral) computational mesh is generated by using ICEM CFD for the intake geometry (Fig. 2). Adaptive mesh refinement (AMR) is performed based on the static temperature gradient to resolve the important phenomena such as shock waves and boundary-layers. The original mesh (prior to mesh adaption), comprises 42,471 cells (430 nodes along with the inlet and leading-edge surface and 100 nodes in the wall-normal directions). The mesh resolution has been determined based on the mesh sensitivity study conducted in a previous study by Ogawa et al. 2010 [8].

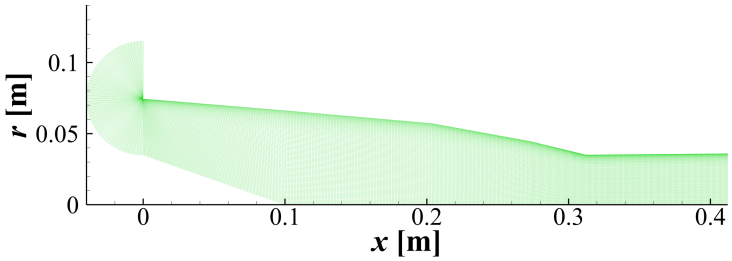

Fig. 2. Computational mesh for the intake geometry

An adaptive mesh sensitivity study is also conducted at Mach 8 to identify the suitable mesh resolution for AMR in terms of the refinement level L, which is the maximum division count for each grid. AMR is also performed based on the static temperature gradient. In this adaptive mesh sensitivity study, the flowfields and flow properties are examined at the maximum refinement level of 7. The flowfields and meshes of L0 and L6 are shown in Fig. 3 for example.

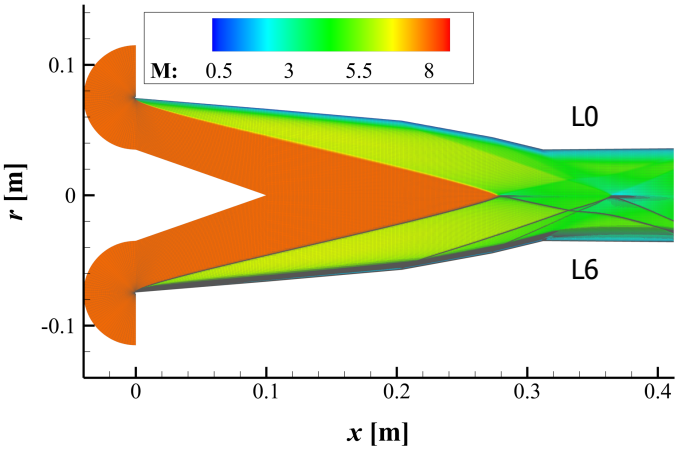

Fig. 3. Flowfields and computational meshes with AMR level of L0 and L6

The pressure distributions on the intake surface are plotted in Fig. 4, which exhibits hardly discernible difference. In addition, stream-thrust averaged flow properties are calculated at the intake exit, as shown in Table 2. The differences among all refinement levels are fractional, where the differences in static pressure and temperature are 0.8% and 1.7%, respectively.

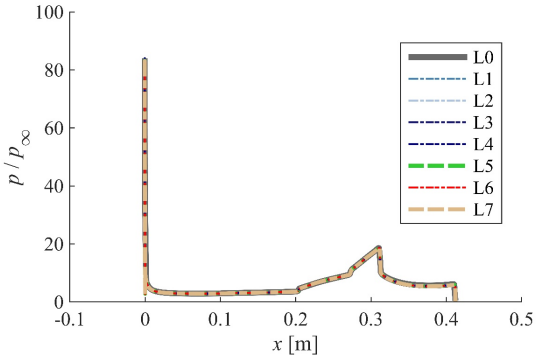

Fig. 4. Pressure distributions on the intake surface at various AMR levels

Table 2. Stream-thrust averaged flow properties at the intake exit at various AMR levels

L	$\bar{M}_2$	$\bar{p}_2$ [Pa]	$\bar{T}_2$ [K]
0	3.89	2.06×10^4	750
1	3.89	2.06×10^4	759
2	3.90	2.06×10^4	763
3	3.90	2.06×10^4	763
4	3.90	2.05×10^4	763
5	3.91	2.05×10^4	762
6	3.91	2.05×10^4	761
7	3.91	2.05×10^4	762

However, a notable difference is observed in the static pressure on the axis of symmetry (centreline) displayed in Fig. 5. The highest compression occurs at the first peak with the refinement level L of 5 due to shock reflection on the centreline, whereas it is marked at the second peak is with the refinement level L of 2. These pronounced peaks are found to occur before the transition of shock reflection configurations, that is, the transition from regular reflection to Mach reflection [11]. Figs. 6 (a) and (b) indicate the occurrence of the transition between the refinement levels 5 and 6 at the point of the first shock impingement and that between the refinement levels 2 and 3 at the point of the second shock

reflection, respectively. Indiscernible difference has been found in the centreline pressure distributions between the AMR levels of L6 and L7. The refinement level of L6 has consequently been deemed sufficient and adaptive mesh refinement is thus conducted by 6 levels in each simulation.

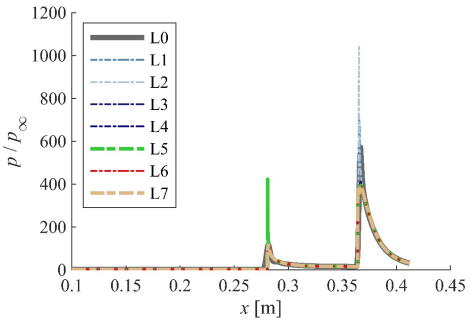

Fig. 5. Pressure distributions on the symmetry axis at various AMR levels

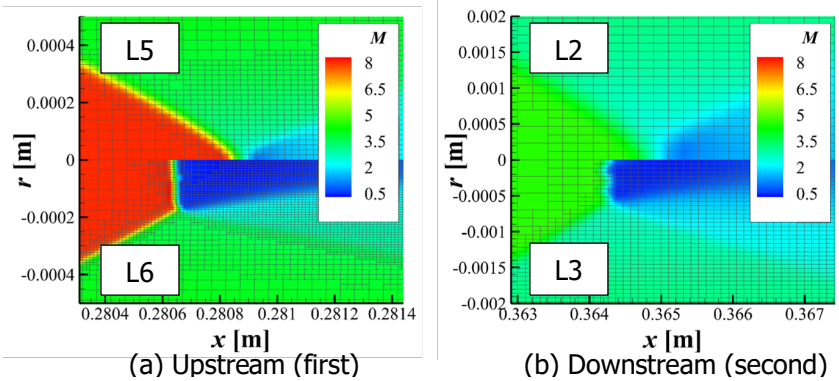

(a) Upstream (first) (b) Downstream (second)

Fig. 6. Transition of upstream (first) and downstream (second) shock reflection on the symmetry axis due AMR levels

The average non-dimensional distance value y^+ of the original mesh is 3.63 and reduced to 0.21 at L6. The minimum cell size is 1.25×10^{-5} m and 8.73×10^{-6} m in the streamwise and wall-normal directions, respectively.

3. Results

3.1. Flowfields

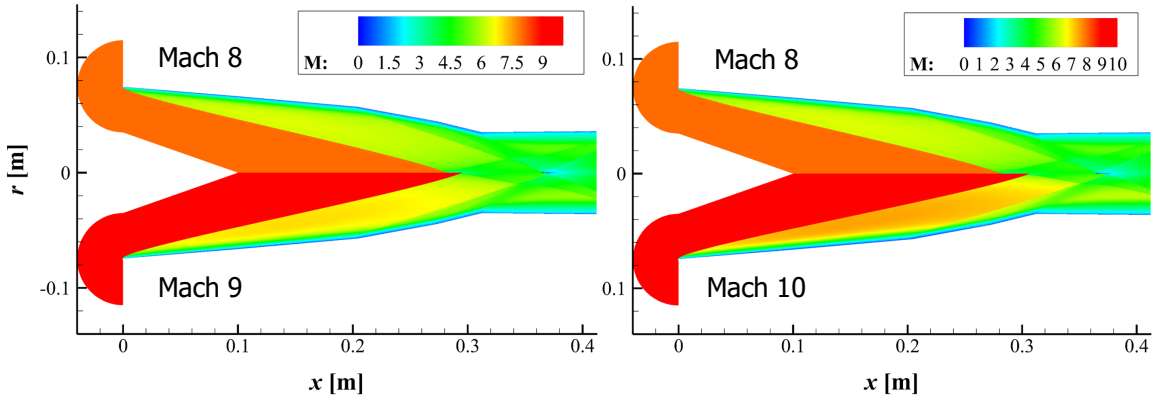

Fig. 7. Mach number distributions at various Mach numbers

The Mach number distributions are displayed at Mach numbers 8, 9 and 10 in Fig. 7. In all cases, two Mach stems have been observed due to the first (upstream) and second (downstream) shock impingement on the symmetry axis. The height of the Mach stem denoted by H (or Mach disk radius) and their non-dimensional value normalised by the intake exit height (radius) r_c are shown in Table 3. The subscript A denotes the first Mach stem and B the second one. It is indicative of considerable influence of the freestream Mach number on the Mach stem height. The subsonic regions downstream

of the Mach stem (disk) are characterised by high temperature and pressure, enabling ignition in the combustor. The static pressure and temperature distributions on the centreline are plotted in Fig. 8. Two peaks correspond to pressure jump across Mach stems in each case. Close inspection of the downstream peaks reveals the presence of two jumps, the first of which is caused by the Mach stem and the second one by compression waves due to incidence of a shock wave into the subsonic region.

Table 3. Mach stem height at various Mach numbers

	Mach 8	**Mach 9**	**Mach 10**
H_A **[m]**	1.66×10^{-4}	1.61×10^{-4}	1.49×10^{-4}
H_A / r_C	4.74×10^{-3}	4.60×10^{-3}	4.26×10^{-3}
H_B **[m]**	6.97×10^{-4}	5.38×10^{-4}	3.92×10^{-4}
H_B / r_C	1.99×10^{-2}	1.54×10^{-2}	1.12×10^{-2}

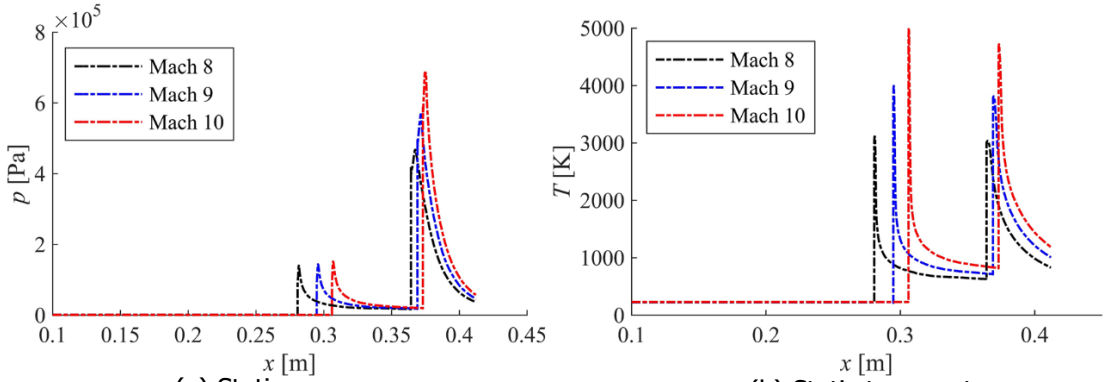

(a) Static pressure (b) Static temperature

Fig. 8. Static pressure and static temperature distributions on the centreline at various Mach numbers

3.2. Temperature at the Intake Exit

The temperature at intake exit is an important attribute that determines the capability of the intake from the viewpoint of supersonic combustion. For radical-farming shock-induced combustion, in particular, appropriate exit temperature is required to achieve stable combustion and to suppress undesirable high-temperature effects. The temperature distributions are plotted in Fig. 9. High-temperature regions are commonly found in the boundary layer at all Mach numbers and downstream of the second Mach reflection at Mach 9 and 10, where the extent of this zone depends on the Mach stem height (Mach stem radius) as per Table 3.

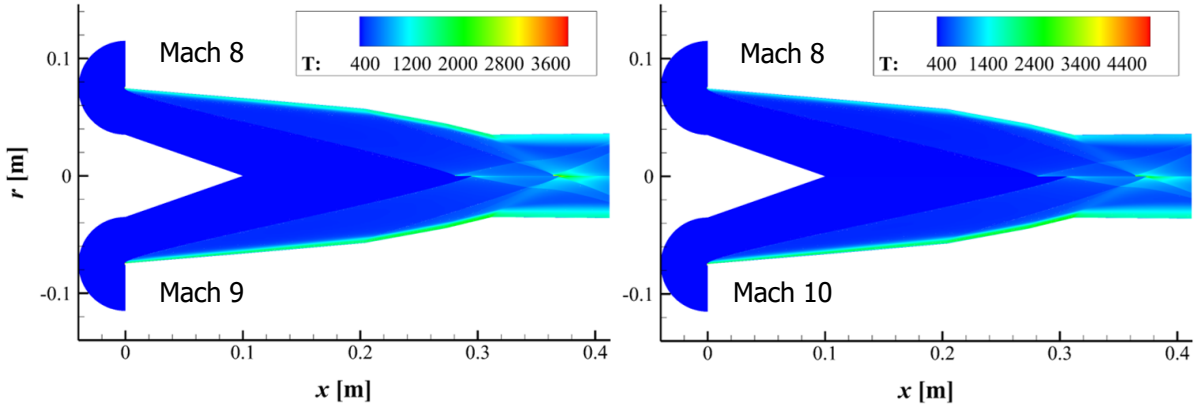

Fig. 9. Static temperature distributions at various Mach numbers

The profiles of the static temperature at the intake exit are plotted in Fig. 10. The mean temperature is calculated by stream-thrust averaging [12,13] so as to evaluate the performance of the intake at

each altitude and Mach number, as shown in Table 4. Minimum temperature of approximately 850 K is required to achieve self ignition with the radical-farming concept [3,4]. The mean temperature is found to be lower than 850 K at Mach 8 while it is locally higher in the boundary layer (Fig. 10). On the other hand, the mean temperature is higher than 850 K at Mach 9 and 10 owing to locally high temperature regions at the centreline due to shock reflection and the wall surface due to viscous effects. It is generally observed that as the higher freestream Mach number, the higher exit temperature as a result of a stronger incident shock wave as well as greater aerodynamic heating.

Table 4. Stream-thrust averaged static temperature at the intake exit

	Mach 8	**Mach 9**	**Mach 10**
$\bar{T}_2$ **[K]**	761	857	968

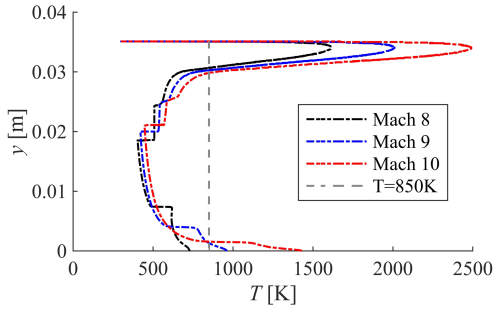

Fig. 10. Static temperature profiles at the intake exit at various Mach numbers

The wall heat flux is determined as a function of the Mach number and static temperature at the edge of the boundary layer, as formulated in Eqs. (1) and (2) with appropriate assumptions.

$$q = k\left(\frac{\partial T}{\partial u}\right)_{y=0} = k\left(\frac{\mathrm{d}T}{\mathrm{d}u}\right)_{y=0}\left(\frac{\partial u}{\partial y}\right)_{y=0} \tag{1}$$

$$\frac{U_\mathrm{e}}{T_\mathrm{e}}\left(\frac{\mathrm{d}T}{\mathrm{d}u}\right)_{y=0} = 1 - \frac{T_\mathrm{w}}{T_\mathrm{e}} + \frac{\gamma - 1}{2}M_\mathrm{e}^2 \tag{2}$$

where q is the wall heat flux and the subscripts e and w denote the edge of boundary layer and wall, respectively.

3.3. Compression efficiency

The compression efficiency η_B is defined relative to adiabatic hence isentropic process, as follows:

$$\eta_\mathrm{B} \equiv \frac{h\left(\bar{T}_{2_{isen}}\right) - h\left(\bar{T}_1\right)}{h\left(\bar{T}_2\right) - h\left(\bar{T}_1\right)} \tag{3}$$

where $\bar{T}_{2_{isen}}$ is calculated by the isentropic relation as

$$\bar{T}_{2_{isen}} = \left(\frac{\bar{p}_2}{\bar{p}_1}\right)^{\frac{\gamma-1}{\gamma}}\bar{T}_1 \tag{4}$$

By definition, for given $\bar{T}_{2_{isen}}$ and $\bar{T}_1$, the greater $\bar{p}_2/\bar{p}_1$, the larger the compression efficiency η_B. The compression efficiency thus represents how efficiently the intake can compress the inflow to a certain temperature between its entrance and exit. The compression efficiency is evaluated using the stream-thrust averaged values.

Table 5 compares the compression efficiency for three flight conditions, along with the stream-thrust averaged values. The compression efficiency is found to be highest at Mach 8 and lowest at Mach 10.

Table 5. Compression efficiency and stream-thrust averaged values at various Mach numbers

	η_B	$\bar{T}_2$ [K]	$\bar{p}_2$ [Pa]	$\bar{p}_{t_2}$ [Pa]
Mach 8	0.681	761	2.05×10^4	2.76×10^6
Mach 9	0.640	857	1.79×10^4	3.54×10^6
Mach 10	0.609	968	1.61×10^4	4.37×10^6

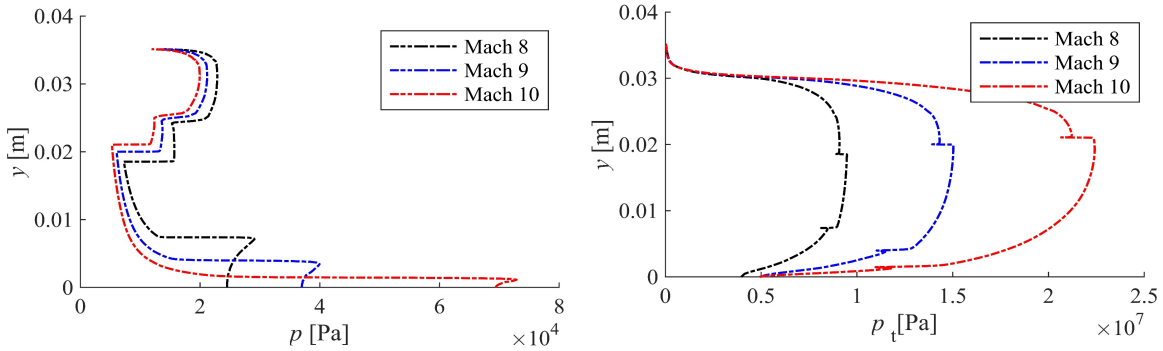

(a) Static pressure (b) Total pressure

Fig. 11. Static temperature and total pressure distributions at the intake exit at various Mach numbers

The static pressure and total pressure distributions at the intake exit are plotted in Fig. 11 for various Mach numbers. Larger total pressure is incurred at higher Mach number due to shock waves and boundary layer. This can be attributed to stronger shock waves and greater aerodynamic heating at higher Mach number, thus indicative of a trade-off tendency between the compression efficiency and the temperature at the intake exit. The total pressure losses normalised by the freestream total pressure are plotted in Fig. 12. It follows that the total pressure loss needs to be reduced to achieve efficient compression at the cost of decreased exit temperature, which can potentially be insufficient for ignition and combustion of the fuel and air mixture downstream.

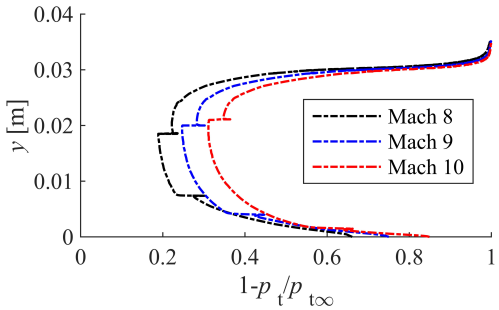

Fig. 12. Total pressure losses at various Mach numbers

3.4. Drag

The intake drag is determined by the pressure and wall shear forces on the wall, as follows:

$$Drag = D_{\text{pressure}} + D_{\text{viscous}} = \int_s (p\sin\theta + \tau\cos\theta)2\pi r \mathrm{d}s \tag{5}$$

The drag is compared in Table 6 for various Mach numbers, along with the breakdown of the pressure and viscous contributions. The distributions of $p \sin\theta$ and $\tau \cos\theta$ along the intake wall are also plotted in Fig. 13.

Table 6. Drag force and component breakdown at various Mach numbers

	$D_{pressure}$ [N]	$D_{viscous}$ [N]	Drag [N]
Mach 8	104.0	17.7	121.7
Mach 9	94.3	17.3	111.6
Mach 10	87.1	16.7	103.8

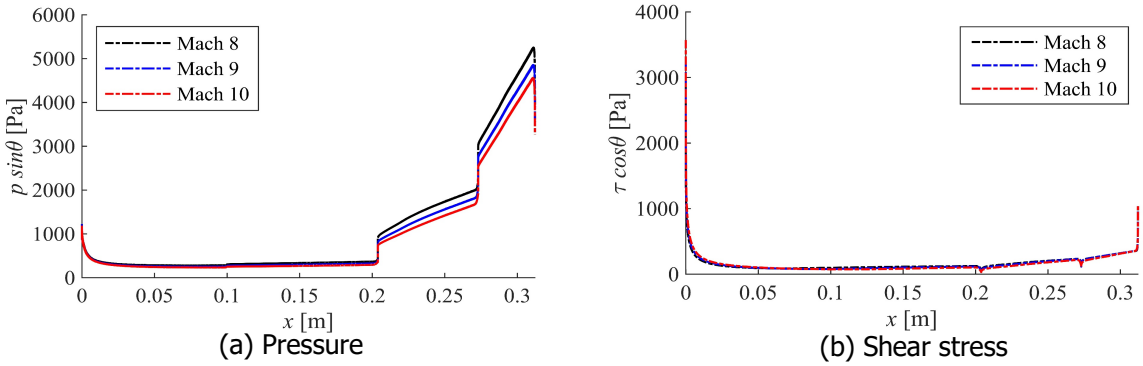

(a) Pressure (b) Shear stress

Fig. 13. Distributions of wall force elements on the intake surface at various Mach numbers

The predominant component of the drag is the pressure force. It is notable that greater drag is incurred at lower altitude on a constant dynamic pressure trajectory even despite large Mach number at lower altitude, which might well yield higher pressure due to stronger shock waves for the same inflow. However, the tendency of the drag observed here is primarily attributed to the freestream condition of constant dynamic pressure. The static pressure is decreased at higher flight Mach number and altitude on the ascent trajectory so as to maintain constant dynamic pressure, as seen in Fig. 14.

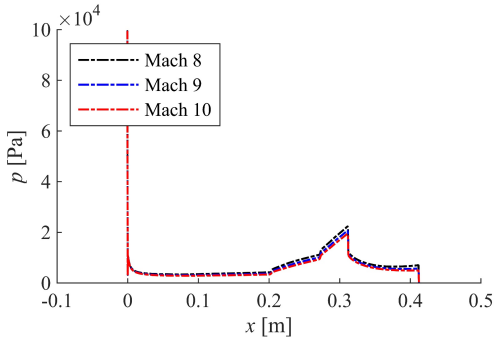

Fig. 14. Static pressure distributions on the intake and part combustor surface at various Mach numbers

The intake drag and exit temperature are examined with respect to the theoretical correlation between them reported in a preceding study [8], as follows:

$$\mathbf{Drag} = \boldsymbol{F}_{\mathbf{in}} - \dot{\boldsymbol{m}} \frac{2\left(\boldsymbol{h}_{\mathbf{t}} + \Delta\boldsymbol{Q}/\dot{\boldsymbol{m}} - \bar{\boldsymbol{h}}_{\mathbf{2}}\right) + \boldsymbol{R}\,\bar{\boldsymbol{T}}_{\mathbf{2}}}{\sqrt{2\left(\boldsymbol{h}_{\mathbf{t}} + \Delta\boldsymbol{Q}/\dot{\boldsymbol{m}} - \bar{\boldsymbol{h}}_{\mathbf{2}}\right)}} \tag{6}$$

where $\boldsymbol{F}_{\mathbf{in}}$ is the stream thrust of the incoming airflow, $\dot{\boldsymbol{m}}$ is the mass flow, $\Delta\boldsymbol{Q}$ is the heat transfer across the intake surface (see Fig. 17 (b)), and $\boldsymbol{h}$ is the enthalpy. Figure 15 indicates good agreement of the numerical results with the theoretical correlation at all Mach numbers.

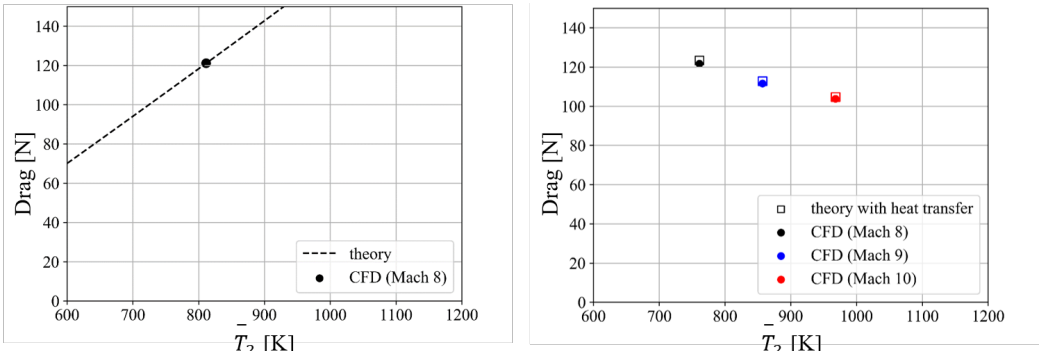

(a) Adiabatic wall (b) Isothermal wall

Fig. 15. Comparison of intake exit temperature vs drag between theory and computation

3.5. Effect of Wall Conditions

The flowfield assuming adiabatic wall condition is compared with that assuming isothermal wall for Mach 8 freestream. Notable difference can be seen particularly in the boundary layer in the static pressure distributions in Fig. 16 (a). The higher surface temperature of the adiabatic wall (Fig. 17) has led to thicker boundary layer, as compared to the isothermal wall case, and subsequently steeper incident shock wave, as shown in the Mach number distributions in Fig. 16 (b).

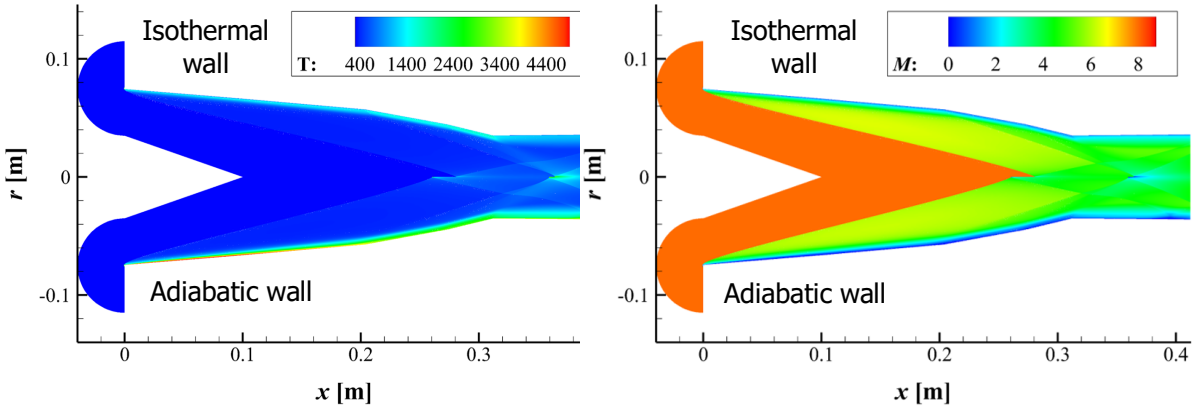

(a) Static temperature (b) Mach number

Fig. 16. Comparison of the flowfields between isothermal and adiabatic wall conditions ($M_\infty = 8$)

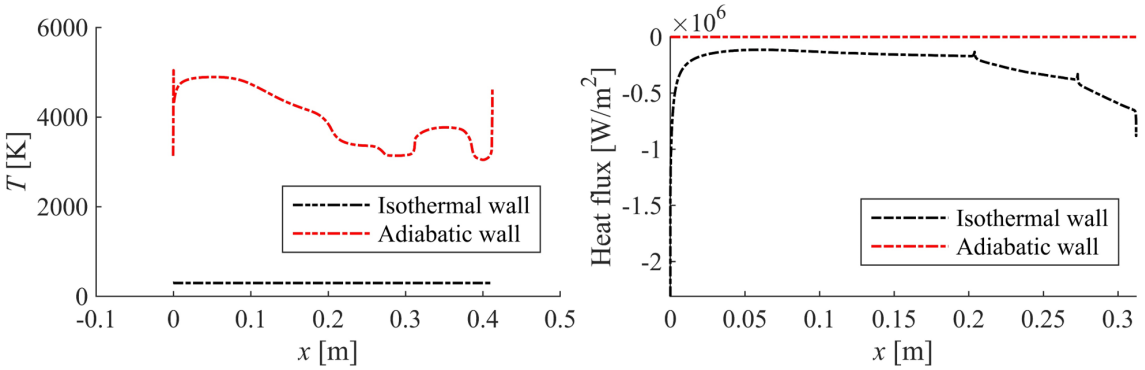

(a) Static temperature (b) Heat flux

Fig. 17. Static temperature and heat flux distributions on the intake surface with isothermal and adiabatic wall conditions

The mean temperature at the intake exit and the compression efficiency are also affected primarily by thicker boundary layer due to higher wall temperature and secondarily by steeper hence stronger incident shock wave. These properties are compared in Table 7.

Table 7. Compression efficiency and stream-thrust averaged flow properties for isothermal and adiabatic wall conditions ($M_\infty = 8$)

	η_B	$\bar{T}_2$ [K]	$\bar{p}_2$ [Pa]	$\bar{p}_{t_2}$ [Pa]
Isothermal wall	0.681	761	2.05×10^4	2.76×10^6
Adiabatic wall	0.649	811	2.19×10^4	2.46×10^6

Table 8 indicates that viscous drag is lower owing to reduced wall shear force in the case of the adiabatic wall condition while the pressure drag is increased due to increased surface pressure, as seen in the distributions of the static pressure and wall shear stress on the intake surface plotted in Fig. 18. Overall, these counteracting effects have resulted in similar total drag force values for these two cases for the Mach 8 freestream but further research is required to examine the intake drag for other flight conditions.

Table 8. Drag force and component breakdown for isothermal and adiabatic wall conditions ($M_\infty = 8$)

	$D_{pressure}$ [N]	$D_{viscous}$ [N]	Drag [N]
Isothermal wall	104.0	17.7	121.7
Adiabatic wall	110.2	11.3	121.2

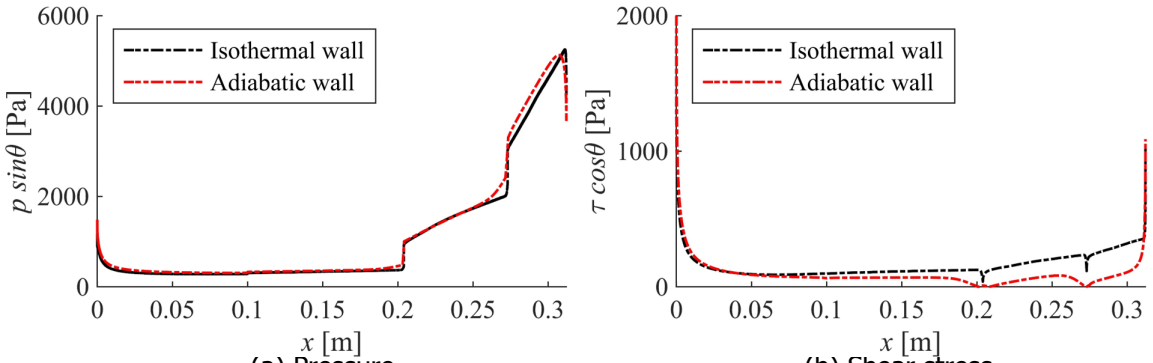

(a) Pressure (b) Shear stress

Fig. 18. Distributions of wall force elements for isothermal and adiabatic wall conditions ($M_\infty = 8$)

3.6. Summary

The insights gained into physical characteristics and relevant parameters such as compression efficiency, drag, and temperature at intake exit are summarised below.

1. Two Mach stems (Mach disks) are observed at the centreline in the intake in all cases, captured by AMR. The Mach stems move downstream as the freestream Mach number increases. These Mach stems generate small subsonic high-temperature regions downstream.
2. The mean temperature calculated by stream-thrust averaging is found to be sufficiently high for self ignition at the intake exit except for the case of Mach 8, where local temperature is adequately high only in the boundary layer.
3. Higher compression efficiency is achieved at lower Mach number while the total pressure loss due to shock waves and boundary layer is larger at higher Mach number. Compression efficiency would need to be traded for higher exit temperature required for ignition.
4. The intake drag becomes smaller at higher altitude on a constant dynamic pressure trajectory. This is mainly due to lower freestream static pressure at higher Mach number for constant dynamic pressure, while wall shear stress exerts rather little influence.

5. The difference in the wall condition assumption primarily affects the boundary layer, leading to lower viscous drag in the case of adiabatic wall. However, overall intake drag remains unchanged, counteracted by increased pressure drag due to steeper shock waves for the Mach 8 freestream condition.

4. Conclusion

The intake flowfields of an axisymmetric scramjet engine are numerically investigated, assuming a typical scramjet operation on a constant dynamic pressure trajectory for scramjet-powered ascent flight from Mach 8 to 10, aiming at access to space. High-fidelity CFD simulation is performed with progressive adaptive mesh refinement to closely resolve the detailed shock configurations.

Substantial pressure increase has been observed upon incident shock impingement on the centreline on the verge of the transition of shock reflection mode in the adaptive mesh refinement study, suggesting the effectiveness of adaptive mesh refinement to accurately capture detailed aerodynamic phenomena including the secondary Mach stem (disk).

The intake performance has been examined with respect to compression efficiency, drag, and mean temperature at the intake exit. While a constant dynamic pressure trajectory is suitably required for scramjet-powered ascent flight in consideration of combustion performance as well as aerothermal and structural limitations, the results indicate the need of careful design for high-performance intakes, taking into account the counteracting characteristics such as the trade-off relation between the compression efficiency and mean temperature at the intake exit. Further, the influence of different wall condition assumptions on the intake drag has been found to be rather insignificant as far as the Mach 8 freestream condition is concerned.

Future research is underway to investigate the effects of angle of attack in an ascending flight and identify key design factors for high-performance intakes for scramjet-powered ascent flight.

References

1. Smart, M. K., Hass, N. E.: Flight Data Analysis of the HyShot 2 Scramjet Flight Experiment, AIAA Journal, 44, 2366-2375 (2006). https://doi.org/10.2514/1.20661
2. McClinton, C.R.: X-43 - Scramjet Power Breaks the Hypersonic Barrier Dryden Lectureship in Research for 2006, 44th AIAA Aerospace Sciences Meeting and Exhibit (2006). https://doi.org/10.2514/6.2006-1
3. Ogawa, H.: Mixing Characteristics of Inclined Fuel injection via Various Geometries for Upstream-Fuel-Injected Scramjets, Journal of Propulsion and Power, 31, 1551-1566 (2015). https://doi.org/10.2514/1.B35581
4. Ogawa, H.: Effects of injection angle and pressure on mixing performance of fuel injection via various geometries for upstream-fuel-injected scramjets, Acta Astronautica, 128, 485-498 (2016). https://doi.org/10.1016/j.actaastro.2016.08.008
5. Odam, J., Paull, A.: Radical Farming in Scramjets. In: Tropea, C., Jakirlic, S., Heinemann, H. J., Henke, R., Hönlinger, H. (eds) New Results in Numerical and Experimental Fluid Mechanics VI. Notes on Numerical Fluid Mechanics and Multidisciplinary Design, 96. Springer, Berlin, Heidelberg (2007). https://doi.org/10.1007/978-3-540-74460-3_34
6. McGuire, J. R., Boyce, R. R., Mudford, N. R.: Radical-Farm Ignition Processes in Two-Dimensional Supersonic Combustion, Journal of Propulsion and Power, 24, 1248-1257 (2012). https://doi.org/10.2514/1.35562
7. Ogawa, H., Grainger, A. L., Boyce, R. R.: Inlet Starting of High-Contraction Axisymmetric Scramjets, Journal of Propulsion and Power, 26, 1247-1258 (2012). https://doi.org/10.2514/1.48284

8. Ogawa, H., Boyce, R. R.: Physical Insight into Scramjet Inlet Behavior via Multi-Objective Design Optimization, AIAA Journal, 50, 1773-1783 (2012). https://doi.org/10.2514/1.J051644
9. ANSYS® Fluent, Release 19.1, Fluent User's Guide ,ANSYS, Inc., (2018).
10. Menter, F. R.: Two-Equation Eddy-Viscosity Turbulence Models for Engineering Applications, AIAA Journal, 32, 1598-1605 (1994). https://doi.org/10.2514/3.12149
11. Ogawa, H., Mölder, S., Timofeev, E.: Numerical Investigation of Mach Reflection Hysteresis in Stunted Busemann Intakes for Axisymmetric Scramjet Engines, 10th International Conference of Flow Dynamics, (2013).
12. Riggins, D. W., McClinton, C. R.: Analysis of Loses in Supersonic Mixing and Reacting Flows, 27th Joint Propulsion Conference, (1991). https://doi.org/10.2514/6.1991-2266
13. Riggins, D. W., McClinton, C. R., Vitt, P. H.: Thrust Losses in Hypersonic Engines Part 1: Methodology, Journal of Propulsion and Power, 13, 281-287 (1997). https://doi.org/10.2514/2.5160